



Reconstructing Primordial Black Hole Power Spectra from Gravitational Waves

Florian Kühnel ^{1,2} and Ioanna Stamou ³

¹*Arnold Sommerfeld Center, Ludwig-Maximilians-Universität, Theresienstraße 37, 80333 München, Germany*

²*Max-Planck-Institut für Physik, Boltzmannstr. 8, 85748 Garching, Germany*

³*Service de Physique Théorique, C.P. 225, Université Libre de Bruxelles, Boulevard du Triomphe, B-1050 Brussels, Belgium*

(Dated: Thursday 11th April, 2024, 12:58am)

A novel methodology for analysing the relation between the energy density in gravitational waves and primordial power spectra is developed. Focusing on scalar-induced gravitational radiation, this methodology is applied to a number of scenarios for the primordial black hole formation. Being differed from conventional Bayesian approaches, its advantages include directness and computational efficiency, which are crucial for handling the complex data characteristic of gravitational wave research. As an important application, it is demonstrated that it allows to systematically identify all scenarios consistent with current and future pulsar-timing-array data.

I. INTRODUCTION

The groundbreaking observations of gravitational waves originating from binary black hole mergers by the LIGO/Virgo collaborations [1–5] has significantly increased interest in both experimental and theoretical investigations of a possible stochastic gravitational-wave background. Importantly, the recent identification of the latter at nano-Hertz frequencies by pulsar timing array (PTA) collaborations [6–8] has generated an avalanche of interest in acquiring understanding of the signal sources [8]. Moreover, the development of future space-based gravitational-wave interferometers such as LISA, BBO and DECIGO [9, 10], alongside ground-based detectors, like Einstein Telescope [11], promises to enable a more comprehensive detection of gravitational waves across a large frequency range.

A variety of theoretical models have been posited as potential sources for the signals detected by PTAs, encompassing phenomena such as scalar-induced gravitational waves [12–14], first-order phase transitions [15–19], cosmic strings [20–23], domain walls [24–27] or primordial black holes (PBHs) [28–32]. A recent comprehensive investigation has explored these theoretical frameworks in depth, offering new insights and perspectives on the origin of PTA signals [8], and numerous of papers have investigated the source of these (see e.g. Ref. [33]).

A large variety of constraints exist on the abundance of PBHs, as extensively reviewed in recent literature (see Ref. [34–36] for reviews). Apart from constraints, there are numerous astrophysical detections which might plausibly be allocated to PBHs (see Ref. [37]). One of the most promising detection methods, accessible with current technology, involves identifying subsolar-mass black holes in compact binary coalescences. Interestingly, recent gravitational-wave observations have reported several subsolar-mass candidate events [38–41]. These findings are far reaching to our understanding of dark matter and early-Universe physics. In particular, they offer insights into the primordial fluctuations that seeded their formation and the nature of dark matter [42, 43].

The present work provides a comprehensive study aimed at studying primordial power spectra from observed gravitational-wave data. Focusing on scalar-induced gravitational waves, and combining theoretical models with simulated observational data, we formulate a novel methodology for the inverse problem in gravitational-wave analysis. Our methodology is distinct from Bayesian statistical approaches, emphasising direct, objective analysis based on empirical data. In order to demonstrate its potential, we explore four specific classes of power spectra: *Broken Power Law*, *Log-Normal Peak* with its variants having *Oscillatory Patterns* or an *UV Cut-Off*. These scenarios have been used to generate datasets of gravitational-wave energy densities, aimed at aligning with the PTA NANOGrav results [28, 33].

Using the corresponding datasets, we reconstruct the scalar power spectra, including the incorporation of noise. Subsequent, we focus on assessing the allowed abundances of PBHs, recalculating the PBH formation thresholds in each case. Finally, we investigate which of these cases effectively reconciles the observed gravitational-wave signals with PBH production. Our analysis suggests that the broken-power-law model is a strong candidate, successfully accounting for gravitational-waves while yielding a substantial fraction of PBH dark matter. While the log-normal scenario and its UV cut-off variant tend to overproduce PBHs, oscillatory patterns can efficiently prevent this.

The structure of this paper is as follow. In Section II we propose a numerical approach to find the power spectrum from the gravitational-wave energy density using fitting techniques. In Section III we apply our analysis to some proposed scenarios having power spectra described by either a broken power law, a log-normal peak, or a log-normal peak with a oscillatory pattern or with a UV cut-off. For the mentioned scenarios, we compute the fractional abundance of PBHs in Section IV. This is followed by a conclusion and outlook in Section V. The Appendix supplements technical details of the evaluation of the gravitational-wave energy density of the scalar power spectrum.

II. METHODOLOGY OF APPROACH FOR INVERSE PROBLEM

This section outlines the methodology used for addressing the inverse problem in the context of scalar-induced gravitational waves. Our approach integrates theoretical power-spectrum models with artificial observational datasets, facilitating the extraction of significant model parameters. Through numerical integration and optimisation methods, we reconcile these theoretical predictions with controlled, simulated data. We detail the steps for generating and analysing artificial observational data, formulating theoretical models, and applying optimisation techniques to refine our understanding of the gravitational-wave signals.

Our primary objective is to design a methodology for optimal fitting of observational data [44]. Contrary to the Bayesian statistical approach extensively explored in the literature (see e.g. Refs. [8, 14, 33, 45–59]), our strategy is anchored in optimisation techniques. This approach emphasises direct and objective analyses based solely on data, without the influence of subjective prior distributions. While Bayesian methods often integrate existing data with prior knowledge, our focus is on a straightforward approach that not only facilitates parameter estimation for theoretical models but can also be extended to more complex fitting techniques. We note that studies with Bayesian analyses using current data are already available (see e.g. Refs. [8, 49]).

Building upon our approach, we present a methodology that stands out for its minimal computational demands, enabling a more efficient exploration of gravitational-wave data, focusing on deriving insights directly from observations without the convolution of subjective priors. This direct, data-centric methodology allows for a more accessible analysis, potentially leveraging advanced computational techniques such as machine learning to unravel the gravitational-wave signals. Through analysing gravitational-wave data, we seek to unveil the origin of these signals, highlighting the significance of primordial black holes.

A. Observational Data

For our analysis, we consider a dataset of n wavenumbers, $k_i = \{k_1, k_2, \dots, k_n\}$, with each wavenumber k_i corresponding to an observational data point w_i^{exp} , representing the observed value of w^{exp} at k_i . Consequently, we formulate a comprehensive dataset represented by

$$\Omega_{\text{GW}}^{\text{exp}}(k) = \{w_1^{\text{exp}}, \dots, w_n^{\text{exp}}\}. \quad (1)$$

Each observational data point w_i^{exp} comes with an associated error σ_i . We remark that, in our present illustrative study, we use simulated data for this process. In our sim-

ulation for the gravitational-wave energy density, Ω_{GW} , we use Gaussian noise to realistically mimic observational errors of actual data.

B. Theoretical Data

In the theoretical framework, we consider a power spectrum model, denoted by $\mathcal{P}_R^{\text{th}}(a; k)$, where a represents a set of parameters that characterises the model. For instance, in a Gaussian case, these parameters would be $a = (\mu, \sigma)$, corresponding to mean (μ) and standard deviation (σ). For each wavenumber k_i within our observational range, we compute the theoretical value $w_i^{\text{th}}(a)$, which corresponds to the gravitational-wave energy density $\Omega_{\text{GW}}(k_i)$ predicted by the model. This process yields a series of values $\Omega_{\text{GW}}^{\text{th}} = \{w_1^{\text{th}}(a), \dots, w_n^{\text{th}}(a)\}$.

The computation of $\Omega_{\text{GW}}(k)$ involves numerical integration over the spectrum of primordial perturbations (a detailed analysis is presented in the Appendix). Due to the integral's complexity and the need for computational efficiency, we apply a numerical integration that approximates the integral as a sum over chosen sample points and their corresponding weights. For our two-dimensional integral, the computation is represented as

$$\Omega_{\text{GW}}(k) = 0.387 \Omega_{\text{R}} \frac{1}{6} \left(\frac{g_{*,s}^4 g_*^{-3}}{106.75} \right)^{-1/3} \times \sum_{i,j=1}^N w_i w_j \mathcal{P}_R \left(\frac{y_j - x_i}{2} k \right) \mathcal{P}_R \left(\frac{x_i y_j}{2} k \right) \overline{I_{\text{RD}}^2(x_i, y_j)}. \quad (2)$$

Here, w_i and w_j are the weights associated with the sampling points as determined by the numerical integration process, specifically using Gaussian quadrature based on the Gauß–Legendre or Gauß–Kronrod quadrature formulae [60, 61]. This approach allows for an accurate estimation of Ω_{GW} , which is essential for a comparison to observational data. We note that a Monte Carlo integration can also give accurate result, but it requires substantially more iterations to obtain similar results. Hence, in order to minimise the computational time, we utilise the aforementioned formulae.

C. Evaluation with Minimisation

Optimising the theoretical model to align with observational data requires a meticulous approach, where we employ the chi-squared χ^2 -function,

$$\chi^2(a) = \sum_{i=1}^n \frac{[w_i^{\text{exp}} - w_i^{\text{th}}(a)]^2}{\sigma_i^2}.$$

The χ^2 -minimisation with respect to parameter vector a is pivotal for extracting the optimal model parameters. We use the Nelder–Mead simplex algorithm [62], being a robust, derivative-free optimisation method. It excels in handling complex, nonlinear problems, especially when derivatives are unavailable or impractical to compute [61, 63]. This algorithm iteratively adjusts a simplex—a geometric figure formed by $N + 1$ points in an N -dimensional parameter space—to converge on the function’s minimum. Whilst it may not be as rapid as gradient-based methods, particularly for high-dimensional problems, its simplicity and versatility make it highly effective in our case, i.e. for models with a moderate number of parameters, offering a balance between reliability and computational efficiency.

III. APPLICATION TO SPECIFIC SCALAR POWER SPECTRA

In this section, we apply our methodology to four distinct models of power spectra. Firstly, we explore the *Broken Power-Law* power spectrum, renowned for its distinct characteristics in single-field inflationary models (cf. Refs. [28, 64]). Secondly, we delve into the standard *Log-Normal* power spectrum, appreciated for its notable features in the abundances of gravitational waves as, for instance, studied in Ref. [33]. Thirdly, our focus shifts to a nuanced variant of the *Log-Normal* model, enhanced by *oscillatory elements*, thus offering enriched insights into gravitational-wave analysis as it was discussed in Ref. [65]. Lastly, we study a specialised form of the *Log-Normal* power spectrum, which integrates an *exponential UV cut-off* (see Ref. [28]).

A. Broken Power-Law

In the context of single-field inflation, peaks are often approximated by a broken-power-law power (PL) spectrum, which is described as

$$\mathcal{P}_{\text{PL}} = A_1 \frac{\alpha_1 + \beta_1}{\beta_1 (k/k_*)^{\alpha_1} + \alpha_1 (k/k_*)^{\beta_1}}. \quad (3)$$

The parameters A_1 and k_* describe the amplitude and position of the peak, respectively, and α_1 and β_1 determine the growth and decay around it. The blue line in Fig. 1 depicts the broken-power-law power spectrum.

In our analysis, we have selected specific parameters for the broken-power-law model: $\alpha = 4$, $\beta = 0.5$, $A = 0.07$, and $k_* = 5 \times 10^7 \text{ Mpc}^{-1}$. This choice is based on their relevance to single-field inflation. Specifically, the hypothesis of adiabatic Gaussian scalar fluctuations, characterised by a power spectrum with simple power-law form, stands as a central prediction of standard slow-roll models, which has been tested with unprecedented accu-

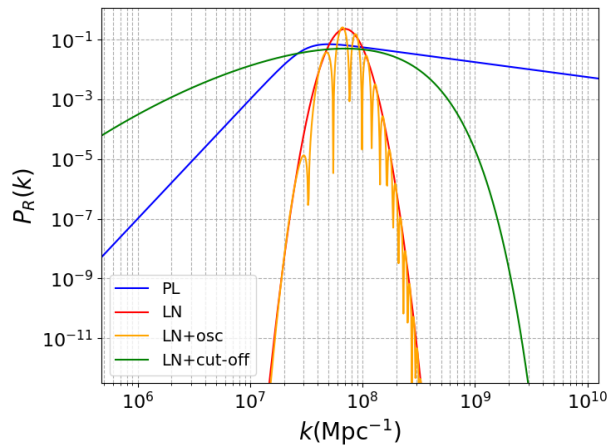


FIG. 1: Power spectrum with the shapes: power law “PL” (blue line), log-normal “LN” (red line), log-normal with oscillations “LN+osc” (orange line) and log-normal with a cut-off “LN+cut-off” (green line). See main text for parameter specification.

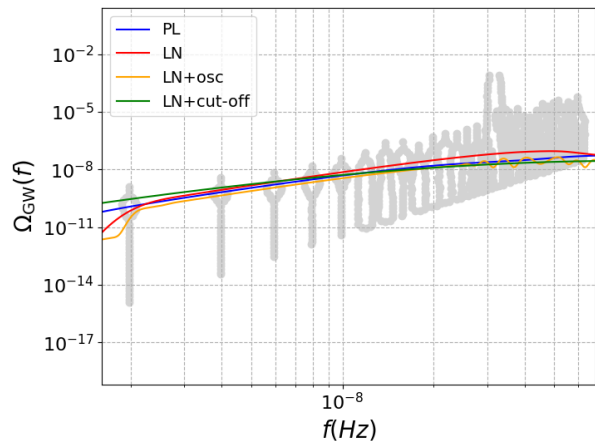


FIG. 2: Energy density for the cases of power law “PL” (blue line), log-normal “LN” (red line), log-normal with oscillations “LN+osc” (orange line) and log-normal with a cut-off “LN+cut-off” (green line). Gray dots corresponds to the NANOGrav signal.

racy [66]. We then compute the integral in Eq. (A19), generating the dataset as described in Eq. (1) and depicted in Figs. 2 and 3, where the blue line represents our results. We note that the energy density from the broken-power law aligns with both the PTA data as well as the detectability range of future observation from LISA and DECIGO (see Fig. 3).

Our fitting process is aimed at an accurate reconstruction of the power spectrum. The corresponding results are shown in Fig. 4 (top-left panel), with the dashed line indicating the fitted values, and the solid line representing those of the exact power spectrum. Our analysis shows consistency between the theoretical model and observed data.

In order to test the resilience of our methodology

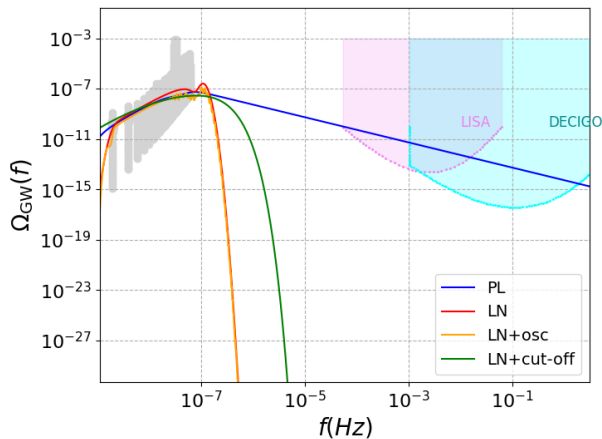


FIG. 3: Energy density for Eqs. (3-6) with blue, red, orange and green color, respectively, as in Fig.2. Gray dots corresponds to NANOGrav signal. Also included are the prospective sensitivity regions of LISA (purple) and DECIGO (cyan).

against data variability, we conduct an analysis which introduces Gaussian noise perturbations into our dataset, simulating observational uncertainties. We apply noise levels of 1% and 10% to assess the impact of varying noise intensities on our results. The effects of these perturbations on the reconstructed power spectra are shown in Fig. 5, with the left panel depicting the 1%-noise scenario and the right panel showing the 10%-noise scenario. We note that order-one noises does not affect the results.

B. Log-Normal Peak

A broad class of power spectra, particularly relevant for primordial black hole formation and gravitational-wave production, can be effectively described using a log-normal (LN) function, relevant in diverse inflationary models (see e.g. Ref. [67]). It can be expressed as

$$\mathcal{P}_{\text{LN}} = \frac{A_2}{\sqrt{2\pi} \Delta} \exp\left(-\frac{\ln^2(k/k_*)}{2\Delta^2}\right). \quad (4)$$

Prior research, particularly in the context of PTA analyses, has identified optimal parameters for this model, these being $\Delta = 0.21$, $A = 0.12$ and $k_* = 7 \times 10^7 \text{ Mpc}^{-1}$ [33]. The corresponding power spectrum is illustrated in Fig. 1 by a red line.

We proceed to calculate the gravitational-wave energy density and establish our dataset accordingly. The latter is graphically represented in Figs. 2 and 3, where the red line corresponds to the outcome for the log-normal model. It can be observed that, while our chosen parameters align well with the PTA data, they diverge from

the expected results at higher frequencies, as previously noted in the study by Ellis *et al.* [33]. This divergence underscores the model's limitations in capturing signals across a broader frequency range

Using our methodology, we successfully reconstruct the power spectrum, the results being showcased in Fig. 4 (upper-right panel). The dashed lines in the figure represent our fitting techniques, while the solid lines indicate the exact data. This comparison highlights the efficacy of our approach. Notably, incorporating varying levels of noise into the data does not significantly change the results (cf. Fig. 6).

C. Log-Normal Peak with Oscillatory Pattern

Extending the investigations of the previous subsection, we introduce an oscillatory pattern to the log-normal distribution. This addition is motivated by multiple factors. First, inflationary potentials featuring step-like characteristics (see e.g. Refs. [68–70]) or those within the context of natural inflation, such as multi-axion field models (see e.g. Refs. [71, 72]), can induce oscillations in the power spectra. Second, oscillatory behavior in the power spectrum can manifest as characteristic signal in the energy densities of gravitational waves [65]. Additionally, such a pattern allows for a more nuanced fit, resembling a comb structure for individual peaks [65]. Finally, as elaborated in the subsequent sections, these oscillations play a crucial rôle in avoiding PBH overproduction [73]. The power spectrum is given by

$$\mathcal{P}_{\text{LN}}^{\text{osc}} = \frac{A_2}{\sqrt{2\pi} \Delta} \exp\left(-\frac{\ln^2(k/k_*)}{2\Delta^2}\right) \cos\left(d \frac{k}{k_*}\right)^2. \quad (5)$$

We retain the parameter values from Eq. (4) while introducing an additional parameter $d = 10$. This value determines the frequency of oscillations in the power spectrum. It also impacts the computational time required to evaluate the energy densities of the gravitational waves. The selected value corresponds to a minimal choice, ensuring that oscillations are present in the energy densities. The power spectrum of Eq. (4) is depicted in Fig. 1 by an orange line.

We compute the gravitational-wave energy density to develop our dataset, being presented in Figs. 2 and 3 by orange lines. These reveal distinct oscillatory patterns in the energy density, reflecting the unique characteristic of this model. Figure 4 (bottom-left panel) shows the successful reconstruction of the power spectrum using our fitting techniques. The dashed line represents the model after the fitting process. As can be seen, our resulting curve closely aligns with the theoretical model.

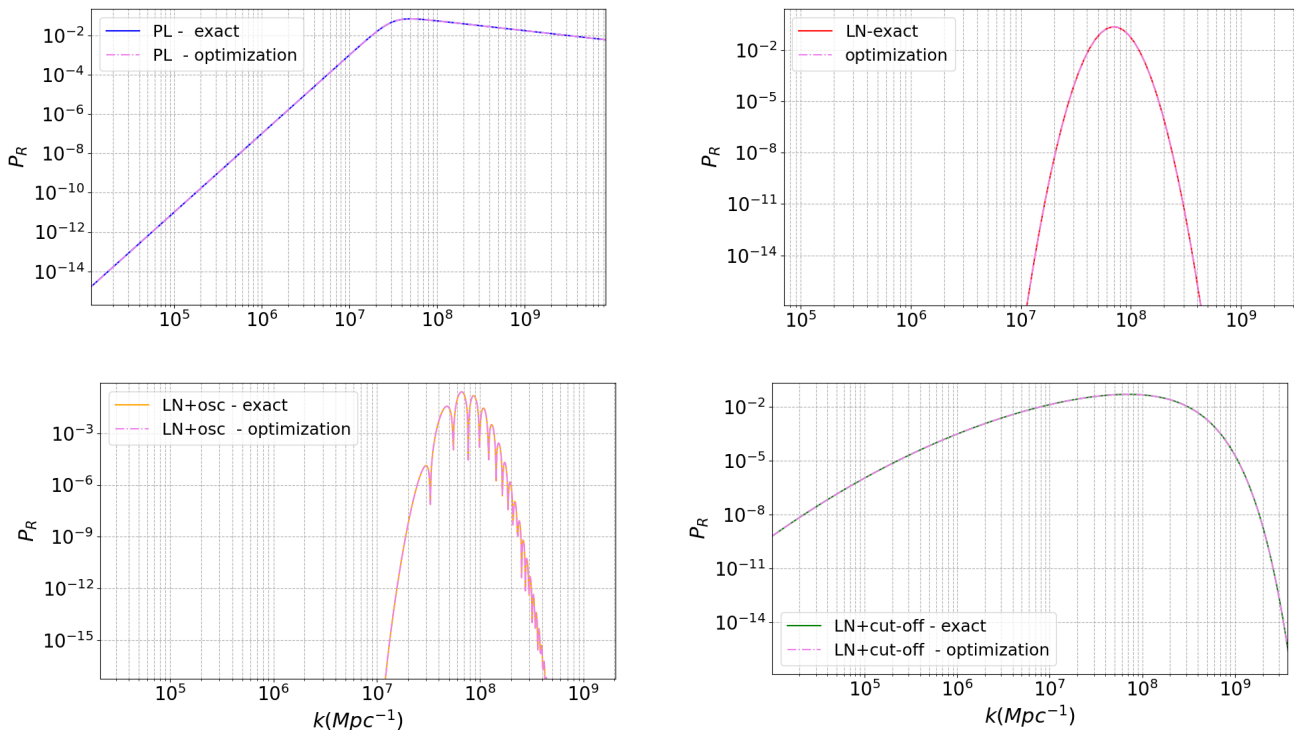


FIG. 4: Power spectra from a given dataset of gravitational waves: broken power law (top-left), log-normal (top-right), log-normal with oscillations (bottom-left) and log-normal with a cut-off (bottom-right).

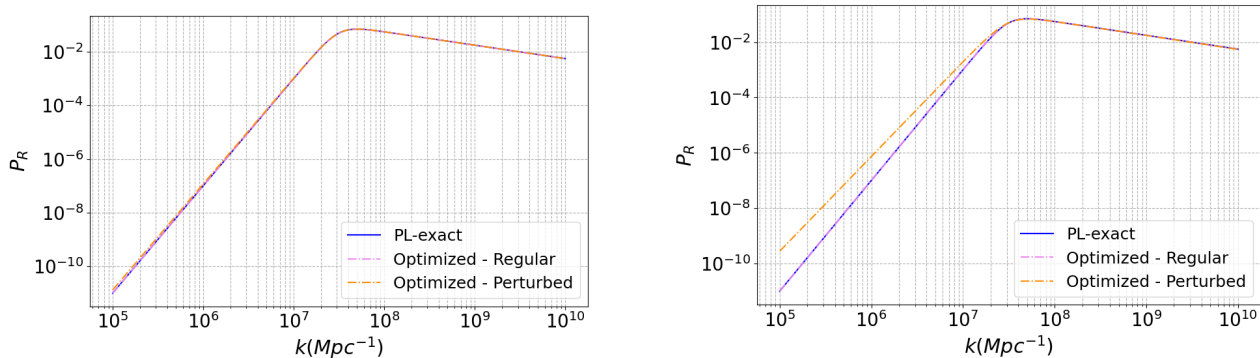


FIG. 5: Power spectra from a given gravitational-wave dataset with 1% (left) and 10% (right) noise.

D. Log-Normal Peak with Exponential UV Cut-Off

A log-normal power spectrum with an exponential UV cut-off has also been studied in Ref. [28]. Here, we assume

$$\mathcal{P}_{\text{LN}}^{\text{cut}} = A_3 \exp \left\{ \beta_2 \left[1 - \frac{k}{k_*} + \ln \left(\frac{k}{k_*} \right) \right] - \alpha_2 \ln^2 \left(\frac{k}{k_*} \right) \right\}. \quad (6)$$

The utilised parameter values correspond to those in Ref. [28]: $\alpha_2 = 0.17$, $\beta_2 = 0.62$, $A_3 = 0.05$, and $k_* = 7 \times 10^7 \text{ Mpc}^{-1}$. The resulting spectrum is shown in Fig. 1 (green line).

As in the previous cases, we obtain our dataset (depicted in Figs. 2 and 3) for the gravitational-wave energy

density. We note that it aligns with the PTA results. Using our fitting techniques, we have reconstructed the power spectrum, as shown in the bottom-right panel of Fig. 4.

Therefore, we have successfully reconstructed the power spectrum from a given dataset for all four models studied above. We remark that a dataset can be analysed using all of the four different models, allowing to accurately identify the most appropriate model for each case. However, for an arbitrary dataset, one needs to incorporate more models, making it hence imperative to proceed to higher optimisation techniques.

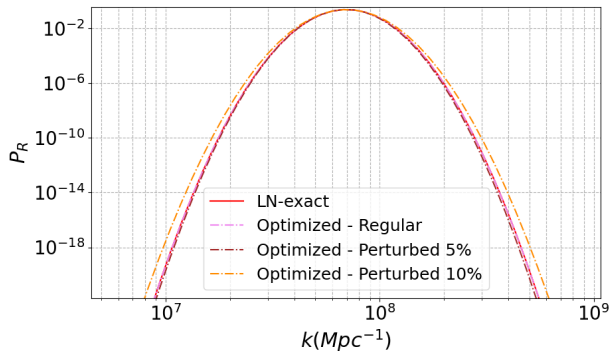


FIG. 6: Power spectra from a given gravitational-wave dataset of with a noise level of 5% (brown dot-dashed curve) and 10% (yellow dot-dashed curve) for the case of a log-normal power spectrum.

IV. GRAVITATIONAL-WAVE BACKGROUND AND PRIMORDIAL BLACK HOLES

In this section, we elaborate on how PBH formation is facilitated by the different power spectra discussed above (see Refs. [28, 30] for similar investigations). As discussed in the literature (see e.g. the recent Refs. [74–78]), the shape of the latter has a vital influence on the former. For each of the power spectra (3–6) we carefully take into account the corresponding PBH formation threshold.

The mass of the PBHs, M , can be related to the wavenumber k by [79–81]

$$M(k) = 10^{18} \left(\frac{\gamma}{0.2} \right) \left(\frac{g_*}{106.75} \right)^{-1/6} \quad (7)$$

$$\times \left(\frac{k}{7 \times 10^{13} \text{ Mpc}^{-1}} \right)^{-2} g, \quad (8)$$

where γ depends upon the details of the gravitational collapse. We use $\gamma = 0.2$ for our analysis as in Ref. [79]. Above, $g_*(T)$ is the effective number of degrees of freedom at the time of PBH formation.

The fraction of collapsed horizon patches, denoted as β , can be estimated using the Press–Schechter (PS) approach [82] or Peak Theory [83]. Our present study concentrates on the former approach, wherein β is determined by the probability that the overdensity δ surpasses a specific collapse threshold, denoted as δ_c . Then, the fraction β is derived from

$$\beta_{\text{PS}}(M) = \frac{1}{2\sqrt{\pi}} \Gamma\left(\frac{1}{2}, \frac{\delta_c^2}{2\sigma^2}\right), \quad (9)$$

where σ is the coarse-grained density constant, given by

$$\sigma^2[M(k)] = \frac{4(1+w)^2}{(5+3w)^2} \int \frac{dk'}{k'} \left(\frac{k'}{k}\right)^4 \mathcal{P}_R(k') \tilde{W}^2\left(\frac{k'}{k}\right), \quad (10)$$

with $\tilde{W}(k'/k)$ being the Fourier transform of the Gaussian window function (see e.g. Ref. [84] for details of how to apply this smoothing function). The choice of the window function introduces corrections in the calculation of the threshold; however, these modifications become less significant in computing the PBH abundance when the same window function is used to evaluate the variations [75, 85, 86].

As obvious from Eq. (9), the fraction β is extremely sensitive to the value of δ_c . In order to address the question of whether the power spectra, given in Eqs. (3–6), can lead to sizeable PBH formation, we carefully evaluate the corresponding thresholds and follow the analytical approach described in Refs. [75, 76, 87]. The threshold calculation necessitates an evaluation of the two-point correlation function, which can be expressed as

$$g(\hat{r}) = \frac{1}{\sigma_0^2} \int_{-\infty}^{\infty} \frac{dk}{k} \frac{\sin(k\hat{r})}{k\hat{r}} \mathcal{P}_R(k). \quad (11)$$

with

$$\sigma_0^2 = \int_{-\infty}^{\infty} \frac{dk}{k} \mathcal{P}_R(k). \quad (12)$$

Equation (11) connects the scalar power spectrum \mathcal{P}_R with the two point correlation function.

For calculating δ_c , it is essential to define the peak value \hat{r}_m of the so-called compaction function C , which has been introduced in Ref. [88], and is defined as

$$C \equiv 2 \frac{M(r, t) - M_b(r, t)}{R(r, t)}, \quad (13)$$

where M is the Misner–Sharp mass and $M_b(r, t) = 4\pi\rho_b R^3/3$. The compaction function can be approximated as [87, 89–91].

$$C \simeq f(w) K(r) r^2 = f(w) \left(1 - [1 + \hat{r} \zeta'(\hat{r})]^2\right), \quad (14)$$

where $f(w) = 3(1+w)/(5+3w)$ and w is the equation-of-state parameter. Here, K and ζ are the conserved comoving curvature perturbations defined on the superhorizon scales. The scale \hat{r}_m is determined through solving the root equation

$$\zeta'(\hat{r}_m) + \hat{r}_m \zeta''(\hat{r}_m) = 0. \quad (15)$$

We introduce the parameter μ as the amplitude of curvature fluctuation, being given as

$$\mu = \zeta(\hat{r})/g(\hat{r}), \quad (16)$$

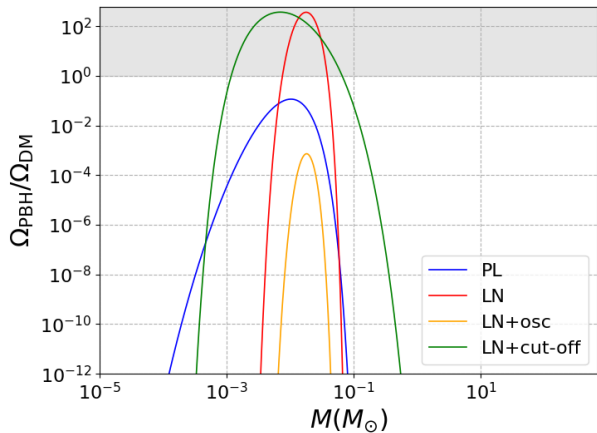


FIG. 7: Fractional PBH abundances for the different models studied in this work.

or, in terms of the compaction function,

$$\mu = \frac{\pm \sqrt{1 - C(\hat{r}_m)/f(w)} - 1}{g'(\hat{r}_m) \hat{r}_m}. \quad (17)$$

The critical amplitude, μ_c , is obtained at $C(r_m) = \delta_c$.

In order to obtain the threshold, we define the function

$$G(\hat{r}_m) = \frac{g'(\hat{r}_m) - \hat{r}_m^2 g'''(\hat{r}_m)/2}{g'(\hat{r}_m)}. \quad (18)$$

The threshold δ_c can then be derived from

$$q = G(r_m) \frac{1}{\sqrt{1 - \delta_c(q)/f(w)}} \frac{1}{\left[1 + \sqrt{1 - \delta_c(q)/f(w)}\right]}, \quad (19)$$

where δ_c is given by

$$\delta_c = \frac{4}{15} e^{-1/q} \frac{q^{1-5/2q}}{\Gamma(5/2q) - \Gamma(5/2q, 1/q)}. \quad (20)$$

The shape parameter q characterises the contour around the peak of the compaction function. Equation (20) provides an analytical method to compute the threshold δ_c as a function of the shape parameter q during the radiation era, as discussed in Ref. [77]. Above, Γ represents the incomplete gamma function.

The abundances of PBHs can be evaluated from [92]

$$\begin{aligned} \frac{\Omega_{\text{PBH}}}{\Omega_{\text{DM}}}[M(k)] &= 1.52 \times 10^8 \left(\frac{\gamma}{0.2}\right)^{3/2} \left(\frac{g_*}{106.75}\right)^{-1/4} \\ &\times \left(\frac{M(k)}{M_\odot}\right)^{-1/2} \beta[M(k)], \end{aligned} \quad (21)$$

| Model | δ_c | f_{PBH} |
|-------------------------|------------|------------------|
| Broken Power-Law | 0.461 | 0.1353 |
| Log-Normal-Peak | 0.466 | 234.01 |
| Log-Normal-Peak+osc | 0.502 | 0.0003 |
| Log-Normal-Peak+cut-off | 0.472 | 580.34 |

TABLE I: Critical thresholds and fractional abundances of PBHs for different models.

and the total abundance of PBHs is given by

$$f_{\text{PBH}} = \int d \ln M \frac{\Omega_{\text{PBH}}}{\Omega_{\text{DM}}}. \quad (22)$$

The resulting PBH abundances for the power spectra studied above are depicted in Fig. 7. The corresponding values of the critical threshold and the fractional abundances to PBHs can be found in Tab. I. The grey region in the figure indicates PBH overproduction. Notably, the broken-power-law model (depicted by the blue line) emerges as a plausible candidate capable of yielding sizeable PBH abundances without overproduction. This conclusion is reinforced by calculations of the critical threshold and fractional PBH abundance derived from the parameters outlined earlier. This model successfully harmonises both the gravitational-wave spectrum and PBH formation, illustrating its potential as a viable theoretical framework.

Contrary to the broken-power-law model, the log-normal peak and its variant with a cut-off—if to explain all of the measured gravitational waves—exhibit a tendency towards PBH overproduction. This can be observed in Fig. 7, where the green and orange lines, corresponding to these models, clearly fall within the grey area indicating excessive PBH production. As before, we evaluate the threshold δ_c in order to produce the fractional abundances of PBHs, the corresponding results being given in Tab. I.

Primordial black hole overproduction in the context of the log-normal power spectrum has also been discussed in Ref. [33]. In the present study, we propose a way to bypass this problem by incorporating oscillations into the power spectrum. This modification can entirely mitigate the overproduction problem as illustrated in Fig. 7 (c.f. orange line). With appropriate choice of the model parameters, it is possible to achieve a dominant contribution to the dark matter fraction without encountering any overproduction.

Finally, we remark that the issue of PBH overproduction remains relatively unchanged across a broad range of the critical threshold values, $\delta_c \in [0.45, 0.51]$. Specifically, this is true for the broken-power-law model. The mass fraction is evaluated using Press–Schechter approach. Incorporating peaks theory into the calculations

affects the results, would lead to larger values for the fractional abundances of PBHs [93–95], these intensifying the problem. We leave a comprehensive discussion to study the effect of incorporating various statistical approaches to future work.

V. CONCLUSION & OUTLOOK

We have proposed a novel methodology to analyse the relation between the energy density in gravitational waves and primordial power spectra. This methodology differs from conventional Bayesian approaches by offering a direct data interpretation. Our study has the advantage of both computational efficiency and simplifying the parametric-space exploration without the need of prior distributions.

As an application, we investigate several scalar power spectra, focusing on four distinct shapes: broken power law, log-normal peak, and its variations incorporating oscillatory patterns and UV cut-offs. Assuming scalar-induced gravitational waves as a full explanation of the recent PTA measurements, we evaluate the associated energy densities and generate datasets suitable for interpreting the PTA signals. Subsequently, we employ optimisation techniques to reconstruct our models. To demonstrate the adaptability of our analysis, we also introduce noise into our dataset. We connect our results to the formation of PBHs. Here, the broken-power-law model stands out for its ability to explain not only the PTA gravitational-wave detection but also for offering an all-PBH explanation to the dark matter problem.

Given the broad applicability of our methodology, we explore the relationship between the energy density of gravitational waves, as described by the various power spectrum shapes, and the abundances of primordial black holes. Knowing that the fractional abundances of primordial black holes strongly depend on the exact value of the threshold at which the fluctuations collapse, we evaluate the threshold for each case. For simplicity, we employ the Press-Schechter approach to evaluate the mass fraction of primordial black holes, using a Gaussian window function for smoothing. Under these assumptions, we find that the broken power-law shape emerges as the most favourable scenario. It not only predicts the signals of various current and future gravitational-wave detections but also accounts for significant dark matter abundances. On the other hand, the log-normal shape cannot explain a broad range of gravitational wave signals and has the significant drawback of yielding overproduction of PBHs. However, by introducing oscillations onto the log-normal shape, this problem can be avoided.

Of course, the studied power-spectrum shapes are rather simple, and realistic PBH models are likely to involve more complex structures. The currently most promising and most natural scenario for PBH formation—the *Thermal History* scenario [96]—extends over

many orders of magnitude in mass and is inherently multimodal. As this can describe around 20 current observations which may be argued to be plausibly attributed to PBHs (see Ref. [37] for the presently most complete overview), we will apply our methodology to investigate the thermal-history power-spectrum shape in a forthcoming study.

Finally, considering the wide applicability of our approach, there are several avenues for application and extension. As regards the former, future work will focus on integrating additional data from forthcoming gravitational-wave observations, including those from LISA and DECIGO. As regards the latter, our approach, suited for extension to other power-spectrum shapes, can well incorporate advantages fitting methods. This specifically includes advanced machine-learning techniques which would enable the exploration of more complex datasets. The training data can be encapsulated in the weights of Eq. (2). Hence, these techniques promise to have potential to identify key features of the signals, thereby deepening our understanding of gravitational waves and their origins—possibly connected to the dark matter in the Universe.

Appendix A: Gravitational Waves

The aim of this section is to provide the basic aspect of the gravitational waves needed in our subsequent analysis. In particular, we show how the energy density of gravitational waves is related to the scalar power spectrum. This section is based on the Refs. [12, 97–100].

1. Equation of Motion for Gravitational Waves

The perturbed metric in conformal Newtonian gauge reads

$$ds^2 = -a^2 (1 + 2\Phi) d\eta^2 + a^2 \left[(1 - 2\Psi) \delta_{ij} + \frac{1}{2} h_{ij} \right] dx^i dx^j, \quad (\text{A1})$$

with η being the conformal time, Φ and Ψ are the Bardeen potential, and h_{ij} is the tensor perturbation, whose equation of motion reads

$$h''_{ij} + 2\mathcal{H} h'_{ij} - \nabla^2 h_{ij} = 2a^2 S_{ij}. \quad (\text{A2})$$

Here, \mathcal{H} represents the conformal Hubble parameter and S_{ij} is the source term. For negligible anisotropic stress, $\Phi = \Psi$, the second-order Einstein tensor and energy-momentum tensor contains the quadratic scalar combinations, which act as a source, which is given by

$$S_{ij} = 4\Phi \partial_i \partial_j \Phi + 2\partial_i \Phi \partial_j \Phi - \frac{4}{3(1+w)} \partial_i \left(\frac{\Phi'}{\mathcal{H}} + \Phi \right) \partial_j \left(\frac{\Phi'}{\mathcal{H}} + \Phi \right). \quad (\text{A3})$$

Upon Fourier transformation,

$$\Phi_{\mathbf{k}}(\eta, \mathbf{k}) = \int d^3x \Phi(\eta, \mathbf{x}) e^{-i\mathbf{k}\cdot\mathbf{x}}, \quad (\text{A4})$$

this becomes

$$S_k^\lambda = \int \frac{d^3k}{(2\pi)^{3/2}} e^{\lambda, ij}(\mathbf{k}) q_i q_j \left[2\Phi_{\mathbf{q}}\Phi_{\mathbf{k}-\mathbf{q}} \right. \\ \left. + \frac{4}{3(1+w)} (\mathcal{H}^{-1}\Phi'_{\mathbf{q}} + \Phi_{\mathbf{q}})(\mathcal{H}^{-1}\Phi'_{\mathbf{k}-\mathbf{q}} + \Phi_{\mathbf{k}-\mathbf{q}}) \right], \quad (\text{A5})$$

where we have used the convolution theorem. With e_{ij}^λ we denote the polarisation modes $\lambda = (+, \times)$ (for further details, see Refs. [12, 100]). Equation (A2) describes the evolution of tensor modes sourced by the scalar perturbations Φ , and is solved by

$$h_k^\lambda(\eta) = \frac{1}{a(\eta)} \int_0^\eta d\tilde{\eta} G_k(\eta, \tilde{\eta}) \alpha(\tilde{\eta}) S_k^\lambda(\tilde{\eta}, \mathbf{k}), \quad (\text{A6})$$

where the Green's function G_k is the solution of

$$G_k''(\eta, \tilde{\eta}) + \left[k^2 - \frac{a''(\eta)}{a(\eta)} \right] G_k(\eta, \tilde{\eta}) = \delta(\eta - \tilde{\eta}). \quad (\text{A7})$$

The Fourier component of the tensor mode is

$$h_{ij}(\eta, \mathbf{x}) = \sum_{\lambda} \int \frac{d^3k}{(2\pi)^{3/2}} h_{\lambda}(\eta, \mathbf{k}) e_{ij}^\lambda(k) e^{i\mathbf{k}\cdot\mathbf{x}}. \quad (\text{A8})$$

As opposed to first order of the Einstein equation, at second order, the scalar, vector and tensor components are not independent. There is a second-order contribution to the tensor mode that depends quadratically on the first-order scalar metric perturbation [97].

The power-spectral density of the tensor perturbation is defined as

$$\langle h_{\mathbf{q}}^\lambda(\eta) h_{\mathbf{k}}^\lambda(\eta) \rangle \equiv \frac{2\pi^2}{k^3} \mathcal{P}_h(\tau, k) \delta^{(3)}(\mathbf{q} + \mathbf{k}), \quad (\text{A9})$$

where $\delta^{(3)}$ is the dimensionless delta distribution. Hence, the power spectrum of the curvature perturbation is

$$\overline{\mathcal{P}_h(t, k)} = \int_0^\infty dv \int_{|1-u|}^{1+u} du T(u, v, \eta, k) \mathcal{P}_R(uk) \mathcal{P}_R(vk), \quad (\text{A10})$$

where T is the transfer function, given by

$$T(u, v, \eta, k) = 4 \left(\frac{4v^2 - (1 + v^2 - u^2)}{4uv} \right)^2 \\ \times \left(\frac{3 + 3w}{5 + 3w} \right)^2 \overline{I^2(u, v, \eta, k)}, \quad (\text{A11})$$

and the kernel function is defined as

$$I(u, v, \eta, k) = \int_0^x dy \frac{a(y/k)}{a(\tau)} k G_k(x, y) f(u, v, \eta, k), \quad (\text{A12})$$

with $x \equiv k\eta$. The oscillation average can be calculated as

$$\overline{I^2(u, v, \eta, k)} \equiv \frac{1}{2\pi} \int_\pi^{x+2\pi} dy^2 I^2(u, v, \eta, k). \quad (\text{A13})$$

Using the variables $t \equiv u + v - 1$ and $s \equiv u - v$, the power spectrum \mathcal{P}_h reads [12]

$$\mathcal{P}_h(\eta, k) = 2 \int_0^\infty dt \int_{-1}^1 ds \left[\frac{t(t+2)(s^2-1)}{(1-s+t)(1+s+t)} \right]^2 \\ \times I^2(u, v, x) \mathcal{P}_R(kv) \mathcal{P}_R(ku), \quad (\text{A14})$$

where the function I is given in terms of u and v (or t and s), assuming that the gravitational waves are produced during radiation- or matter-dominated era.

2. Gravitational-Wave Energy Density

The fraction of the gravitational-wave energy density per logarithmic wavelength is obtained via

$$\Omega_{\text{GW}}(\eta, k) = \frac{\rho_{\text{GW}}(\eta, k)}{\rho_{\text{tot}}(k)} = \frac{1}{24} \left(\frac{k}{a(\eta)H(\eta)} \right)^2 \overline{\mathcal{P}_h(\eta, k)}, \quad (\text{A15})$$

where

$$\rho_{\text{GW}}(\eta, k) = \frac{M_{\text{Pl}}^2}{8} \frac{k^2}{\alpha^2} \overline{\mathcal{P}_h(\eta, k)}. \quad (\text{A16})$$

We study two cases of radiation- and matter-dominated Universe.

Assuming that the power spectrum of gravitational waves is produced in the radiation-dominated era yields the solution

$$\overline{I_{\text{RD}}^2(u, v, x \rightarrow \infty)} = \frac{1}{2} \left(\frac{3(u^2 + v^2 - 3)}{4u^3 v^3 x} \right)^2 \\ \times \left[\left(-4uv + (u^2 + v^2 - 3) \log \left| \frac{3 - (u+v)^2}{3 - (u-v)^2} \right| \right)^2 \right. \\ \left. + \pi^2 (u^2 + v^2 - 3)^2 \Theta(v + u - \sqrt{3}) \right], \quad (\text{A17})$$

or, in t, s variables,

$$\overline{I_{\text{RD}}^2(t, s, x \rightarrow \infty)} = \frac{288 (s^2 + t(2+t) - 5)^2}{x^2 (1-s+t)^6 (1+s+t)^6}$$

$$\begin{aligned} & \times \left\{ \frac{\pi^2}{4} \left(s^2 + t(t+2) - 5 \right)^2 \Theta \left[t - \left(\sqrt{3} - 1 \right) \right] \right\} \\ & + \left[\frac{1}{2} \left[s^2 + t(t+2) - 5 \right] \log \left| \frac{(2+t)t-2}{3-s^2} \right| \right. \\ & \quad \left. + (s-1-t)(t+s+1) \right]^2. \end{aligned} \quad (\text{A18})$$

For the gravitational-wave energy density, one obtains

$$\begin{aligned} \Omega_{\text{GW}}(k) &= 0.387 \Omega_{\text{R}} \left(\frac{g_{*,s}^4 g_*^{-3}}{106.75} \right)^{-1/3} \frac{1}{6} \frac{(y^2-1)(x^2-1)}{(x-y)^2(x+y)^2} \\ & \times \int_{-1}^1 dx \int_1^\infty dy \mathcal{P}_R \left(\frac{y-x}{2} k \right) \mathcal{P}_R \left(\frac{x+y}{2} k \right) \overline{I_{\text{RD}}^2(x,y)}, \end{aligned} \quad (\text{A19})$$

where $x = s$ and $y = t + 1$. Here, Ω_{R} is the radiation abundance ($\Omega_{\text{R}} = 5.38 \times 10^{-5}$), and g_* and $g_{*,s}$ are the effective degrees of freedom for the energy and entropy densities, respectively. They can be approximately considered to be equal.

In a matter-dominated Universe, the function $I(u, v, x)$ is given by

$$I_{\text{MD}}(u, v, x) = \frac{6(x^3 + 3x \cos x - 3 \sin x)}{5x^3}, \quad (\text{A20})$$

and for the oscillation average $\overline{I_{\text{MD}}^2(v, u, x \rightarrow \infty)} = 18/25$. In this work we focus on the energy density of gravitational waves in the radiation-dominated era.

-
- [1] B. P. Abbott *et al.* (LIGO Scientific, Virgo), *Phys. Rev. Lett.* **116**, 061102 (2016), arXiv:1602.03837 [gr-qc].
- [2] B. P. Abbott *et al.* (LIGO Scientific, VIRGO), *Phys. Rev. Lett.* **118**, 221101 (2017), [Erratum: *Phys.Rev.Lett.* 121, 129901 (2018)], arXiv:1706.01812 [gr-qc].
- [3] B. P. Abbott *et al.* (LIGO Scientific, Virgo), *Astrophys. J. Lett.* **851**, L35 (2017), arXiv:1711.05578 [astro-ph.HE].
- [4] B. P. Abbott *et al.* (LIGO Scientific, Virgo), *Phys. Rev. Lett.* **119**, 141101 (2017), arXiv:1709.09660 [gr-qc].
- [5] B. P. Abbott *et al.* (LIGO Scientific, Virgo), *Phys. Rev. Lett.* **116**, 241103 (2016), arXiv:1606.04855 [gr-qc].
- [6] G. Agazie *et al.* (NANOGrav), *Astrophys. J. Lett.* **951**, L8 (2023), arXiv:2306.16213 [astro-ph.HE].
- [7] G. Agazie *et al.* (NANOGrav), *Astrophys. J. Lett.* **951**, L9 (2023), arXiv:2306.16217 [astro-ph.HE].
- [8] A. Afzal *et al.* (NANOGrav), *Astrophys. J. Lett.* **951**, L11 (2023), arXiv:2306.16219 [astro-ph.HE].
- [9] P. Amaro-Seoane *et al.* (LISA), (2017), arXiv:1702.00786 [astro-ph.IM].
- [10] K. Yagi and N. Seto, *Phys. Rev. D* **83**, 044011 (2011), [Erratum: *Phys.Rev.D* 95, 109901 (2017)], arXiv:1101.3940 [astro-ph.CO].
- [11] M. Maggiore *et al.*, *JCAP* **03**, 050, arXiv:1912.02622 [astro-ph.CO].
- [12] K. Kohri and T. Terada, *Phys. Rev. D* **97**, 123532 (2018), arXiv:1804.08577 [gr-qc].
- [13] V. Acquaviva, N. Bartolo, S. Matarrese, and A. Riotto, *Nucl. Phys. B* **667**, 119 (2003), arXiv:astro-ph/0209156.
- [14] S. Vagnozzi, *JHEAp* **39**, 81 (2023), arXiv:2306.16912 [astro-ph.CO].
- [15] K. Fujikura, S. Girmohanta, Y. Nakai, and M. Suzuki, *Phys. Lett. B* **846**, 138203 (2023), arXiv:2306.17086 [hep-ph].
- [16] A. Addazi, Y.-F. Cai, A. Marciano, and L. Visinelli, *Phys. Rev. D* **109**, 015028 (2024), arXiv:2306.17205 [astro-ph.CO].
- [17] E. Megias, G. Nardini, and M. Quiros, *Phys. Rev. D* **108**, 095017 (2023), arXiv:2306.17071 [hep-ph].
- [18] L. Zu, C. Zhang, Y.-Y. Li, Y.-C. Gu, Y.-L. S. Tsai, and Y.-Z. Fan 10.1016/j.scib.2024.01.037 (2023), arXiv:2306.16769 [astro-ph.HE].
- [19] M. W. Winkler and K. Freese, (2024), arXiv:2401.13729 [astro-ph.CO].
- [20] J. Ellis, M. Lewicki, C. Lin, and V. Vaskonen, *Phys. Rev. D* **108**, 103511 (2023), arXiv:2306.17147 [astro-ph.CO].
- [21] N. Kitajima and K. Nakayama, *Phys. Lett. B* **846**, 138213 (2023), arXiv:2306.17390 [hep-ph].
- [22] G. Lazarides, R. Maji, and Q. Shafi, *Phys. Rev. D* **108**, 095041 (2023), arXiv:2306.17788 [hep-ph].
- [23] A. Eichhorn, R. R. Lino dos Santos, and J. a. L. Miqueleto, *Phys. Rev. D* **109**, 026013 (2024), arXiv:2306.17718 [gr-qc].
- [24] N. Kitajima, J. Lee, K. Murai, F. Takahashi, and W. Yin, (2023), arXiv:2306.17146 [hep-ph].
- [25] S.-Y. Guo, M. Khlopov, X. Liu, L. Wu, Y. Wu, and B. Zhu, (2023), arXiv:2306.17022 [hep-ph].
- [26] S. Blasi, A. Mariotti, A. Rase, and A. Sevrin, *JHEP* **11**, 169, arXiv:2306.17830 [hep-ph].
- [27] Y. Gouttenoire and E. Vitagliano, (2023), arXiv:2306.17841 [gr-qc].
- [28] V. Vaskonen and H. Veermäe, *Phys. Rev. Lett.* **126**, 051303 (2021), arXiv:2009.07832 [astro-ph.CO].
- [29] G. Franciolini, A. Iovino, Junior., V. Vaskonen, and H. Veermäe, *Phys. Rev. Lett.* **131**, 201401 (2023), arXiv:2306.17149 [astro-ph.CO].
- [30] K. Inomata, K. Kohri, and T. Terada, (2023), arXiv:2306.17834 [astro-ph.CO].

- [31] Y.-F. Cai, X.-C. He, X.-H. Ma, S.-F. Yan, and G.-W. Yuan, *Sci. Bull.* **68**, 2929 (2023), arXiv:2306.17822 [gr-qc].
- [32] S. Wang, Z.-C. Zhao, J.-P. Li, and Q.-H. Zhu, (2023), arXiv:2307.00572 [astro-ph.CO].
- [33] J. Ellis, M. Fairbairn, G. Franciolini, G. Hütsi, A. Iovino, M. Lewicki, M. Raidal, J. Urrutia, V. Vasikonen, and H. Veermäe, *Phys. Rev. D* **109**, 023522 (2024), arXiv:2308.08546 [astro-ph.CO].
- [34] B. Carr, F. Kuhnel, and M. Sandstad, *Phys. Rev. D* **94**, 083504 (2016), arXiv:1607.06077 [astro-ph.CO].
- [35] B. Carr, K. Kohri, Y. Sendouda, and J. Yokoyama, *Rept. Prog. Phys.* **84**, 116902 (2021), arXiv:2002.12778 [astro-ph.CO].
- [36] B. Carr and F. Kuhnel, *SciPost Phys. Lect. Notes* **48**, 1 (2022), arXiv:2110.02821 [astro-ph.CO].
- [37] B. Carr, S. Clesse, J. Garcia-Bellido, M. Hawkins, and F. Kuhnel, *Phys. Rept.* **1054**, 1 (2024), arXiv:2306.03903 [astro-ph.CO].
- [38] R. Abbott *et al.* (LIGO Scientific, VIRGO, KAGRA), *Phys. Rev. Lett.* **129**, 061104 (2022), arXiv:2109.12197 [astro-ph.CO].
- [39] K. S. Phukon, G. Baltus, S. Caudill, S. Clesse, A. Depasse, M. Fays, H. Fong, S. J. Kapadia, R. Magee, and A. J. Tanasijczuk, (2021), arXiv:2105.11449 [astro-ph.CO].
- [40] R. Abbott *et al.* (LIGO Scientific, VIRGO, KAGRA), *Mon. Not. Roy. Astron. Soc.* **524**, 5984 (2023), [Erratum: *Mon. Not. Roy. Astron. Soc.* 526, 6234 (2023)], arXiv:2212.01477 [astro-ph.HE].
- [41] G. Morras *et al.*, *Phys. Dark Univ.* **42**, 101285 (2023), arXiv:2301.11619 [gr-qc].
- [42] M. Prunier, G. Morrás, J. F. N. n. Siles, S. Clesse, J. García-Bellido, and E. Ruiz Morales, (2023), arXiv:2311.16085 [gr-qc].
- [43] A. L. Miller, N. Aggarwal, S. Clesse, F. De Lillo, S. Sachdev, P. Astone, C. Palomba, O. J. Piccinni, and L. Pierini, (2024), arXiv:2402.19468 [gr-qc].
- [44] A. Roper Pol, C. Caprini, A. Neronov, and D. Semikoz, *Phys. Rev. D* **105**, 123502 (2022), arXiv:2201.05630 [astro-ph.CO].
- [45] Z. Yi, Q. Gao, Y. Gong, Y. Wang, and F. Zhang, *Sci. China Phys. Mech. Astron.* **66**, 120404 (2023), arXiv:2307.02467 [gr-qc].
- [46] G. Domènech, S. Pi, A. Wang, and J. Wang, (2024), arXiv:2402.18965 [astro-ph.CO].
- [47] Z.-C. Chen, J. Li, L. Liu, and Z. Yi, (2024), arXiv:2401.09818 [gr-qc].
- [48] G. Agazie *et al.* (International Pulsar Timing Array), (2023), arXiv:2309.00693 [astro-ph.HE].
- [49] A. Mitridate, D. Wright, R. von Eckardstein, T. Schröder, J. Nay, K. Olum, K. Schmitz, and T. Trickle, (2023), arXiv:2306.16377 [hep-ph].
- [50] Z.-Q. You, Z. Yi, and Y. Wu, *JCAP* **11**, 065, arXiv:2307.04419 [gr-qc].
- [51] W. Handley and P. Lemos, *Phys. Rev. D* **103**, 063529 (2021), arXiv:2007.08496 [astro-ph.CO].
- [52] A. Ashok, P. B. Covas, R. Prix, and M. A. Papa, (2024), arXiv:2401.17025 [gr-qc].
- [53] M. Breschi, R. Gamba, G. Carullo, D. Godzieba, S. Bernuzzi, A. Perego, and D. Radice, (2024), arXiv:2401.03750 [astro-ph.HE].
- [54] J. C. Aurrekoetxea, C. Hoy, and M. Hannam, (2023), arXiv:2312.03860 [gr-qc].
- [55] T. Gupta and N. J. Cornish, *Phys. Rev. D* **109**, 064040 (2024), arXiv:2312.11808 [gr-qc].
- [56] M. Hübner, C. Talbot, P. D. Lasky, and E. Thrane, *Phys. Rev. D* **101**, 023011 (2020), arXiv:1911.12496 [astro-ph.HE].
- [57] A. Matas and J. D. Romano, *Phys. Rev. D* **103**, 062003 (2021), arXiv:2012.00907 [gr-qc].
- [58] M. Benetti, L. L. Graef, and S. Vagnozzi, *Phys. Rev. D* **105**, 043520 (2022), arXiv:2111.04758 [astro-ph.CO].
- [59] W. G. Lamb, S. R. Taylor, and R. van Haasteren, *Phys. Rev. D* **108**, 103019 (2023), arXiv:2303.15442 [astro-ph.HE].
- [60] R. Piessens, E. D. Doncker-Kapenga, C. Uberhuber, and D. K. Kahaner, *Springer series in computational mathematics* (1983).
- [61] W. H. Press, S. A. Teukolsky, W. T. Vetterling, and B. P. Flannery, (1996).
- [62] J. A. Nelder and R. Mead, *Computer Journal* **7**, 308 (1965).
- [63] P. Desesquelles, T. M. H. Ha, A. Korichi, F. Le Blanc, and C. M. Petrache, *J. Phys. G* **36**, 037001 (2009), arXiv:0902.3814 [nucl-ex].
- [64] C. T. Byrnes, P. S. Cole, and S. P. Patil, *JCAP* **06**, 028, arXiv:1811.11158 [astro-ph.CO].
- [65] J. Fumagalli, S. e. Renaux-Petel, and L. T. Witkowski, *JCAP* **08**, 059, arXiv:2105.06481 [astro-ph.CO].
- [66] Y. Akrami *et al.* (Planck), *Astron. Astrophys.* **641**, A10 (2020), arXiv:1807.06211 [astro-ph.CO].
- [67] S. Pi and M. Sasaki, *JCAP* **09**, 037, arXiv:2005.12306 [gr-qc].
- [68] J. A. Adams, B. Cresswell, and R. Easther, *Phys. Rev. D* **64**, 123514 (2001), arXiv:astro-ph/0102236.
- [69] K. Kefala, G. P. Kodaxis, I. D. Stamou, and N. Tetradis, *Phys. Rev. D* **104**, 023506 (2021), arXiv:2010.12483 [astro-ph.CO].
- [70] Y.-F. Cai, X.-H. Ma, M. Sasaki, D.-G. Wang, and Z. Zhou, *Phys. Lett. B* **834**, 137461 (2022), arXiv:2112.13836 [astro-ph.CO].
- [71] G. Ballesteros, J. Rey, and F. Rompineve, *JCAP* **06**, 014, arXiv:1912.01638 [astro-ph.CO].
- [72] N. E. Mavromatos, V. C. Spanos, and I. D. Stamou, *Phys. Rev. D* **106**, 063532 (2022), arXiv:2206.07963 [hep-th].
- [73] J. L. Cook, *JCAP* **07**, 031, arXiv:2209.05674 [astro-ph.CO].
- [74] I. Musco, *Phys. Rev. D* **100**, 123524 (2019), arXiv:1809.02127 [gr-qc].

- [75] I. Musco, V. De Luca, G. Franciolini, and A. Riotto, *Phys. Rev. D* **103**, 063538 (2021), arXiv:2011.03014 [astro-ph.CO].
- [76] A. Escrivà, C. Germani, and R. K. Sheth, *JCAP* **01**, 030, arXiv:2007.05564 [gr-qc].
- [77] A. Escrivà, C. Germani, and R. K. Sheth, *Phys. Rev. D* **101**, 044022 (2020), arXiv:1907.13311 [gr-qc].
- [78] I. D. Stamou, *Phys. Rev. D* **108**, 063515 (2023), arXiv:2306.02758 [astro-ph.CO].
- [79] B. J. Carr, *Astrophys. J.* **201**, 1 (1975).
- [80] B. J. Carr and S. W. Hawking, *Mon. Not. Roy. Astron. Soc.* **168**, 399 (1974).
- [81] G. Ballesteros and M. Taoso, *Phys. Rev. D* **97**, 023501 (2018), arXiv:1709.05565 [hep-ph].
- [82] W. H. Press and P. Schechter, *The Astrophysical Journal* **187**, 425 (1974).
- [83] J. M. Bardeen, J. Bond, N. Kaiser, and A. Szalay, *Astrophys. J.* **304**, 15 (1986).
- [84] A. Kalaja, N. Bellomo, N. Bartolo, D. Bertacca, S. Matarrese, I. Musco, A. Raccanelli, and L. Verde, *JCAP* **10**, 031, arXiv:1908.03596 [astro-ph.CO].
- [85] S. Young, *Int. J. Mod. Phys. D* **29**, 2030002 (2019), arXiv:1905.01230 [astro-ph.CO].
- [86] K. Tokeshi, K. Inomata, and J. Yokoyama, *JCAP* **12**, 038, arXiv:2005.07153 [astro-ph.CO].
- [87] A. Escrivà, F. Kuhnel, and Y. Tada, (2022), arXiv:2211.05767 [astro-ph.CO].
- [88] M. Shibata and M. Sasaki, *Phys. Rev. D* **60**, 084002 (1999), arXiv:gr-qc/9905064.
- [89] T. Harada, C.-M. Yoo, T. Nakama, and Y. Koga, *Phys. Rev. D* **91**, 084057 (2015), arXiv:1503.03934 [gr-qc].
- [90] A. G. Polnarev and I. Musco, *Class. Quant. Grav.* **24**, 1405 (2007), arXiv:gr-qc/0605122.
- [91] A. G. Polnarev, T. Nakama, and J. Yokoyama, *JCAP* **09**, 027, arXiv:1204.6601 [gr-qc].
- [92] K. Inomata, M. Kawasaki, K. Mukaida, Y. Tada, and T. T. Yanagida, *Phys. Rev. D* **96**, 043504 (2017), arXiv:1701.02544 [astro-ph.CO].
- [93] S. Young, C. T. Byrnes, and M. Sasaki, *JCAP* **07**, 045, arXiv:1405.7023 [gr-qc].
- [94] Q. Wang, Y.-C. Liu, B.-Y. Su, and N. Li, *Phys. Rev. D* **104**, 083546 (2021), arXiv:2111.10028 [astro-ph.CO].
- [95] I. D. Stamou, *Phys. Rev. D* **103**, 083512 (2021), arXiv:2104.08654 [hep-ph].
- [96] B. Carr, S. Clesse, J. García-Bellido, and F. Kühnel, *Phys. Dark Univ.* **31**, 100755 (2021), arXiv:1906.08217 [astro-ph.CO].
- [97] D. Baumann, P. J. Steinhardt, K. Takahashi, and K. Ichiki, *Phys. Rev. D* **76**, 084019 (2007), arXiv:hep-th/0703290.
- [98] S. Mollerach, D. Harari, and S. Matarrese, *Phys. Rev. D* **69**, 063002 (2004), arXiv:astro-ph/0310711.
- [99] M. Maggiore, *Phys. Rept.* **331**, 283 (2000), arXiv:gr-qc/9909001.
- [100] J. R. Espinosa, D. Racco, and A. Riotto, *JCAP* **09**, 012, arXiv:1804.07732 [hep-ph].